Supporting Information

Engineering a layered-differentiation core-shell architecture: $NiCoAlO_x$@Pt/ZSM-5 for synergistically enhanced activity and dual H_2O/SO_2 resistance in propane oxidation

Shixing Wu[a, b#], Qian Peng[a, c#], Chao Feng[d], Haitao Zhang[e], Zhifang Zhou[c*], Fang Dong[a*], Zhicheng Tang[a*]

(a. National Engineering Research Center for Fine Petrochemical Intermediates, State Key Laboratory of Low Carbon Catalysis and Carbon Dioxide Utilization, Lanzhou Institute of Chemical Physics, Chinese Academy of Sciences, Lanzhou 730000, China;

b. University of Chinese Academy of Sciences, Beijing 100039, China;

c. School of Metallurgy and Environment, Lanzhou University of Technology, Lanzhou 730050, China;

d. College of Chemical and Biological Engineering, Shandong University of Science and Technology, Qingdao, Shandong 266590, China;

e. Lanzhou Petrochemical Research Center, Petrochemical Research Institute, PetroChina, Lanzhou 730060, China.)

[#]These authors contributed equally: Shixing Wu, Qian Peng.

---

[*]Corresponding author.

E-mail address: zhouzf@lut.edu.cn (Z. Zhou), dongfang@licp.cas.cn (F. Dong), tangzhicheng@licp.cas.cn (Z. Tang).

1. Chemical reagents

Nickel nitrate hexahydrate ($Ni(NO_3)_2·6H_2O$), cobalt nitrate hexahydrate ($Co(NO_3)_2·6H_2O$), aluminum nitrate hydrate ($Al(NO_3)_2·9H_2O$), chloroplatinic acid hexahydrate ($H_2PtCl_6·6H_2O$), sodium hydroxide (NaOH) and *n*-butylamine ($C_4H_{11}N$) were purchased from Xilong Chemical Co. Ltd., Chengdu Cologne Chemical Co. Ltd., Xilong Science Co. Ltd., Chengdu Cologne Chemical Co. Ltd., Beijing Beihua Fine Chemicals Co. Ltd. and Shanghai McLean Biochemical Technology Co. Ltd., respectively. Water glass ($Na_2O·nSiO_2$) was composed of 250 g/L SiO_2, 90 g/L Na_2O and water. Ethanol was purchased from LianlongBohua (Tianjin) Pharmaceutical Chemicals Co. Ltd. and distilled water was made in the laboratory. All chemical materials were analytically pure reagents and used without further purification.

2. Experimental

2.1. Synthesis of $Pt/Ni_aCo_bAlO_x$ catalysts

For the synthesis of $Pt/Ni_1Co_{0.5}AlO_x$ catalyst, $Ni(NO_3)_2·6H_2O$ (3.102 g, 10.67 mmol), $Co(NO_3)_2·6H_2O$ (1.552 g, 5.33 mmol) and $Al(NO_3)_2·9H_2O$ (1.999 g, 5.33 mmol) were dissolved in 20 mL of deionized water under ultrasonic agitation for 10 min to form solution A. Separately, H_2PtCl_4 solution (38.6 mmol/L, 1.00 mL) and NaOH (1.366 g, 34.15 mmol) were ultrasonically dissolved in another 20 mL of deionized water to form solution B.

2.2. Synthesis of $Pt/Ni_1Co_{0.5}AlO_x$@ZSM-5(5%) catalyst

To synthesize the ZSM-5 shell with a 5 wt% loading, water glass (0.333 g) and *n*-butylamine (0.026 g) were dissolved in 10 mL of distilled water and stirred vigorously for 10 min (solution C). Simultaneously, $Pt/Ni_1Co_{0.5}AlO_x$ core (1.430 g) was dispersed

in another 10 mL of distilled water to form a homogeneous suspension (suspension D). Suspension D was then added dropwise to solution C under vigorous stirring at room temperature for 30 min, followed by the addition of an extra 10 mL of distilled water and continued stirring for 1.5 h.

2.3. Synthesis of $Ni_1Co_{0.5}AlO_x$@Pt/ZSM-5(3%), $Ni_1Co_{0.5}AlO_x$@Pt/ZSM-5(5%) and $Ni_1Co_{0.5}AlO_x$@Pt/ZSM-5(10%) catalysts

The $Ni_1Co_{0.5}AlO_x$ core was synthesized via the same procedure as the $Pt/Ni_1Co_{0.5}AlO_x$ catalyst, except that no H_2PtCl_4 solution was added to solution B during the preparation of the $Ni_1Co_{0.5}$Al-LDH precursor. Additionally, 1.00 mL of H_2PtCl_4 solution was introduced into suspension D to achieve a theoretical Pt loading of 0.5 wt% for all samples. Specifically, to prepare $Ni_1Co_{0.5}AlO_x$@Pt/ZSM-5(3%), (5%), and (10%), the dosages of water glass, *n*-butylamine and $Ni_1Co_{0.5}AlO_x$ core were (0.184 g, 0.014 g and 1.455 g), (0.333 g, 0.026 g and 1.430 g) and (0.700 g, 0.054 g and 1.350 g), respectively.

3. Catalytic performance measurements

The catalytic activity and stability of the catalysts for VOCs oxidation were evaluated in a fixed-bed continuous-flow reactor using propane as the probe molecule. For the activity tests, 400 mg of catalyst (20-40 mesh, obtained by pressing and sieving) was thoroughly mixed with 200 mg of SiO_2. The mixture was loaded into the isothermal zone (packed with quartz wool) of a quartz reactor tube (length: 30 cm; inner diameter: 8 mm). A reactant gas stream containing 2000 ppm propane in air was introduced at a flow rate of 200 mL/min, corresponding to a weight hourly space velocity (WHSV) of

30000 mL·g^{-1}·h^{-1}. The catalytic reaction was conducted at various temperatures, and the concentrations of reactants and products were monitored online using a gas chromatograph (FULI GC9790II) equipped with a flame ionization detector (FID). Propane conversion and CO_2 selectivity were calculated based on the measured concentrations using the standard equations.

$$X_{C_3H_8} = \frac{[C_3H_8]_{in} - [C_3H_8]_{out}}{[C_3H_8]_{in}} \times 100\%$$

$$CO_2\ selectivity = \frac{[CO_2]_{out}}{([C_3H_8]_{in} - [C_3H_8]_{out}) \times 3} \times 100\%$$

Here, $X_{C_3H_8}$, $[C_3H_8]_{in}$, $[C_3H_8]_{out}$ and $[CO_2]_{out}$ represented conversion of propane, inlet concentration of propane, outlet concentration of propane, and outlet concentration of CO_2, respectively. The catalytic stability test followed the same procedure as the activity test, except that the reaction temperature was maintained to ensure a high propane conversion (85.0-95.0%) for a long time.

4. Catalyst characterizations

The morphology of the catalysts was analyzed by transmission electron microscopy (TEM, JEOL-JEM-2010). Brunauer-Emmett-Teller (BET) surface area, the pore size, and the pore volume of the catalysts were obtained by adsorption and desorption of nitrogen in the ASAP 2020 instrument (America Micromeritics). Raman scattering was done by using a Laboratory Human Resources Evolution Raman spectrometer (BX41). The crystal phases of each element in the catalyst were determined by an X-ray diffraction instrument (XRD, Japan Smartlabse) (scanning angle of 10°-90°, scanning speed of 0.5°/min, 60 kV, 55 mA) under the radiation of λ

= 1.5406 nm. The Fourier transform infrared spectroscopy (FTIR) analysis of the samples was performed using a Fourier infrared spectrometer (Nexus 870, Nicolet), and ATR technology was used for FTIR analysis. Infrared spectra were tested with a Nicolet Nexus 870 Fourier transform infrared spectrometer. X-ray photoelectron spectroscopy (XPS) measurements were performed with a Thermo Scientific 250 Xi Electron Spectrometer (Mg Kα radiation; hν = 1253.6 eV). The multifunctional dynamic adsorption instrument TP-5080-D was used to analyze the redox behavior, surface acidity, and oxygen species characteristics of the catalyst surface. For H_2-TPR, a 50 mg sample was heated from room temperature to 900 ^oC in reduced gas with volume fractions of 5 vol % H_2 and 95 vol % N_2, and the detector signal was continuously recorded. For the O_2-TPD test, the catalyst (50 mg) was pretreated with nitrogen (99.9%) for 1 h at 300 ^oC. When the temperature dropped to 50 ^oC, the O_2 (5% O_2/N_2) adsorption was carried out for 60 min. After the adsorption was over, purged for 0.5 h, and the desorbed O_2 signal was detected at 50-900 ^oC. The temperature-programmed desorption operation of NH_3-TPD was similar to that of O_2-TPD, except that O_2 was changed to NH_3 and the desorbed NH_3 signal was detected at 50-800 ^oC. The H_2-TPR data in Fig. S13 were calibrated by pure CuO as a standard. The following reaction equation shows that 1 mol CuO consumes 1 mol H_2. We performed H_2-TPR tests on CuO of different masses to obtain H_2 consumption and peak area. The peak area (Y) and H_2 consumption (X) were linearly fitted to obtain the linear equation shown in Fig. S13. The peak area obtained by the TPR peak fitting of different catalysts was put into the equation to obtain the H_2 consumption.

$$CuO + H_2 = Cu + H_2O \quad (1)$$

In-situ diffuse reflectance infrared Fourier transform spectroscopy (DRIFTS) spectra of reaction behaviors of C_3H_8 over the $Ni_1Co_{0.5}AlO_x$@Pt/ZSM-5(3%) catalyst under both air and SO_2-containing atmospheres were collected using a VERTEX 70 spectrometer equipped with an MCT detector and a CaF_2 window in-situ cell. The DRIFTS cell served as the reaction chamber, and spectra were collected in the frequency range of 4000-600 cm^{-1}. For C_3H_8 oxidation under air, a total of 200 mg of catalyst (40-60 mesh) was packed into the DRIFTS cell. Firstly, the catalyst was pretreated at 400 ^oC by flowing N_2 for 30 minutes. After cooling to 40 ^oC, the catalyst was exposed to a C_3H_8/Ar gas mixture containing 2000 ppm C_3H_8 at a flow rate of 30 mL/min until adsorption saturation was achieved. Subsequently, N_2 was introduced to purge the weakly adsorbed species. Lastly, N_2 was switched to 20% O_2/N_2 mixture with a flow rate of 30 mL/min and the catalyst was oxidized at different temperatures (100 ^oC, 150 ^oC, 200 ^oC, 250 ^oC, 300 ^oC, and 350 ^oC) with a heating rate of 10 ^oC/min, during which the spectra were recorded. For C_3H_8 oxidation under SO_2-containing atmosphere, the experimental procedure was identical to that under air, except that the reaction gas was replaced with air containing 30 ppm SO_2 after N_2 purging.

Supplementary analysis concerning BET in the manuscript is as follows:

The Pt/$Ni_1Co_{0.5}AlO_x$@ZSM-5(5%), $Ni_1Co_{0.5}AlO_x$@Pt/ZSM-5(5%), and $Ni_1Co_{0.5}AlO_x$@Pt/ZSM-5(10%) catalysts exhibited combined type I/IV isotherms with H4 hysteresis loops. The I and IV combined isotherms indicated both the microporosity and mesoporosity, and H4 hysteresis loop represented narrow slit-shaped pores usually

found in solids with a mixture of microporous and mesoporous, demonstrating that $Pt/Ni_1Co_{0.5}AlO_x$@ZSM-5(5%), $Ni_1Co_{0.5}AlO_x$@Pt/ZSM-5(5%) and $Ni_1Co_{0.5}AlO_x$@Pt/ZSM-5(10%) catalysts were composites of ZSM-5 and hydrotalcite-derived oxides.

5. Kinetic studies

The catalytic performance could also be identified by kinetic studies, such as apparent activation energy (E_a), which is measured as follows:

$$lnr = \frac{-E_a}{RT} + C \tag{2}$$

In equation (2), r represents the reaction rate ($mol \cdot g^{-1} \cdot s^{-1}$), T refers to the reaction temperature, and C is a constant term.

$$r = \frac{F_{Propane} \times X_{Propane}}{W} \tag{3}$$

In equation (3), $X_{Propane}$ denotes the conversion of C_3H_8, $F_{Propane}$ indicates the feeding rate ($mol \cdot s^{-1}$), and W corresponds to the mass of the catalyst. Therefore, the plots of lnr and 1000/T yield the E_a value.

The kinetic studies also include specific reaction rates, such as the catalyst's mass (R_m) and the catalyst's specific surface area (R_s), which were calculated using the following equations:

$$\eta_{Propane} = log\frac{1}{1 - \frac{X_{Propane}}{100}} \tag{4}$$

$$R_S = \frac{F \times \eta_{Propane}}{S} \tag{5}$$

$$R_m = \frac{F \times \eta_{Propane}}{W} \tag{6}$$

Turnover frequency (TOF), defined as the number of C_3H_8 molecules converted per active site per second, was calculated according to the equation:

$$TOF_{Pt} = \frac{F_{Propane} \times X_{Propane}}{\frac{m_{Cat} \times x(Pt)}{M_{Pt}} \times d(Pt)} \tag{7}$$

$$TOF_{Ni} = \frac{F_{Propane} \times X_{Propane}}{\frac{m_{Cat} \times x(Ni)}{M_{Ni}} \times d(Ni)} \tag{8}$$

$$TOF_{Co} = \frac{F_{Propane} \times X_{Propane}}{\frac{m_{Cat} \times x(Co)}{M_{Co}} \times d(Co)} \tag{9}$$

Where $F_{propane}$ is the C_3H_8 flow rate (mol/s), $X_{propane}$ is the conversion of C_3H_8, m_{Cat} is the mass of the catalyst (g), M_{Pt}, M_{Ni}, M_{Co} (g/mol) are the malar of Pt (195.05 g/mol), Ni (58.69 g/mol), Co (58.93 g/mol), respectively; d(Pt), d(Ni) and d(Co) are the dispersions of Pt, Ni and Co, which are calculated from the ratios of Pt^0/Pt_{total}, Ni^{3+}/Ni_{total} and Co^{3+}/Co_{total} in the XPS spectra, respectively; x(Pt), x(Ni) and x(Co) are the total contents of Pt, Ni and Co in various samples (obtained by XPS experiments), respectively.

6. Theoretical calculations

All calculations were performed using the density functional theory (DFT) technique using the Vienna ab initio simulation package (VASP). Spin-polarized calculations were performed using the generalized gradient approximation (GGA) combined with the Perdew-Burke-Ernzerhof (PBE) method to determine the exchange and correlation energies. The projector-augmented wave (PAW) method was used to

represent the core–valence electron interactions. The typical plane-wave cutoff energy was 400 eV for basis-set expansion. For geometry optimization calculations, forces were converged below 0.03 eV/Å. The SCF convergence energy was 1×10^{-4} eV. A1 × 1 × 1 k-point mesh was used to perform all the calculations.

For simulating the Pt/NiAlCoO structure, a three-layer slab model surface of $NiAl_2O_4$ (101) substitution was built to calculate the adsorption energies and Gibbs free energies. Three p (3 × 3) unit cell expansions with some Co and Ni atoms instead of Al were used to model the surface of NiAlCoO. And the same Pt structure was supported to simulate Pt/NiAlCoO structures. Similarly, for the Pt/NiAlCoO/ZSM structure, a three-layer slab model surface of MFI structure substitution was built to calculate the adsorption energies and Gibbs free energies. Three p (3 × 3) unit cell expansions with (001) surface cut were used to model the surface of ZSM. The same Pt atoms and NiAlCoO structure were both supported on ZSM, which is named Pt/NiAlCoO/ZSM. A vacuum of 15 Å was used to simulate the surface under periodic boundary conditions.

The adsorption energy (E_{ads}) of the H_2O, Propane and the other molecule on the surface was calculated as follows (eq 1):

$$E_{ads} = E_{adsorbate+surface} - E_{surface} - E_{gas}, \quad (1)$$

where $E_{surface}$ is the clean surface relaxation energy of the surface slab, E_{gas} is the energy of a free gas molecule under conditions of vacuum, and $E_{adsorbate+surface}$ is the energy of the composite system.

According to the definition of ΔG,[1-3]

$$\Delta G = \Delta E + \Delta E_{ZPE} - T\Delta S + \Delta G_U + \Delta G_{pH} + \Delta G_{field} \quad (11)$$

ΔE is directly calculated by DFT.

ΔE_{ZPE} is obtained by calculating the vibration frequency of the intermediate (the ZPE corrects for the vibration of the adsorbate at 0 K). Due to the conservation of elements before and after each calculation step, in the calculation, ΔE_{ZPE} can be approximated as 0.

Because of the temperature we defined as 0 K, $T\Delta S = 0$.[4]

ΔG_{pH} is the contribution of H^+ concentration change to the Gibbs free energy. Due to the absence of pH changes in the gas-solid reaction, it can be ignored as 0.[5]

ΔG_U is the contribution of free energy in electrode potential. Electrocatalysis is not involved in this experiment, so it is ignored.

The correction term for electric double-layer free energy, known as ΔG_{field}, has a negligible effect on overall free energy and can be ignored.[3]

For model optimization and simulation of reactions under ER and LH mechanisms, the calculations are performed at 0 K at a fixed cell volume, the differences in the Gibbs free energy should equal the differences in the total energy. However, the MvK mechanism was acquired under high temperature; the calculated temperature was set as 800 K. By this definition, a negative value of E_{ads} corresponds to exothermic and spontaneous adsorption processes.

The barrier energy, ΔE, for a difference between the transition state energy and standard product formation enthalpy is defined as follows. The energy barrier calculation of *-$CH_3CH_2CH_3$ and *-O to *-$CH_3CH_2OHCH_3$ on Pt/NiAlCoO as an example (eq 2):

$$\Delta E = \left(E_{CH3CH2CH3+O-Pt/NiAlCoO} - E_{stab-Pt/NiAlCoO}\right) - \left(E_{CH3CH2OHCH3-Pt/N}\right) \quad (2)$$

where $E_{CH3CH2CH3+O-Pt/NiAlCoO}$ and $E_{CH3CH2OHCH3-Pt/NiAlCoO}$ are the energies of the *-$CH_3CH_2CH_3$+O* and *-$CH_3CH_2OHCH_3$ on Pt/NiAlCoO, $E_{stab-Pt/NiAlCoO}$ is the energy of the Pt/NiAlCoO surface slab.

The differences in the Gibbs free energy should equal the differences in the total energy. By this definition, the lower the ΔE is, the easier it is to react.

Fig. S1. TEM images of $Pt/Ni_1Co_{0.5}AlO_x$ (a and b), $Pt/Ni_1Co_{0.5}AlO_x$@ZSM-5(5%) (c and d), $Ni_1Co_{0.5}AlO_x$@Pt/ZSM-5(3%) (e and f), $Ni_1Co_{0.5}AlO_x$@Pt/ZSM-5(5%) (g and h) and $Ni_1Co_{0.5}AlO_x$@Pt/ZSM-5(10%) (i and j) catalysts.

Fig. S2. HRTEM images of $Pt/Ni_1Co_{0.5}AlO_x$ (a and b), $Pt/Ni_1Co_{0.5}AlO_x$@ZSM-5(5%) (c and d), $Ni_1Co_{0.5}AlO_x$@Pt/ZSM-5(3%) (e and f), $Ni_1Co_{0.5}AlO_x$@Pt/ZSM-5(5%) (g and h) and $Ni_1Co_{0.5}AlO_x$@Pt/ZSM-5(10%) (i and j) catalysts.

Fig. S3. The catalytic activity of $Pt/Ni_aCo_bAlO_x$ catalysts.

Fig. S4. Characteristic temperatures (T_{10}, T_{50} and T_{90}) of propane oxidation on $Pt/Ni_1Co_{0.5}AlO_x$ and its core-shell catalysts under dry air (a) and 5 vol% H_2O (b) conditions.

Fig. S5. Catalytic activity of $Pt/Ni_1Co_{0.5}AlO_x$ and $Ni_1Co_{0.5}AlO_x$@Pt/ZSM-5(3%) catalysts under dry air and 5 vol% H_2O conditions.

Fig. S6. E_a and reaction rate versus T_{90} of $Pt/Ni_1Co_{0.5}AlO_x$ and its core-shell catalysts under dry air (a) and 5 vol% H_2O (b) conditions.

Fig. S7. R_s (reaction rates based on the specific area of catalysts) and R_m (reaction rates based on the mass of catalysts) of $Pt/Ni_1Co_{0.5}AlO_x$ and its core-shell catalysts under dry air and 5 vol% H_2O conditions.

Fig. S8. TOF_{Pt} (a), TOF_{Ni} (b) and TOF_{Co} (c) values of $Pt/Ni_1Co_{0.5}AlO_x$ and its core-shell catalysts under dry air and 5 vol% H_2O conditions.

Fig. S9. TOF_{Pt} (f) of $Pt/Ni_1Co_{0.5}AlO_x$ and its core-shell catalysts under dry air conditions.

Fig. S10. The thermal stability of $Pt/Ni_1Co_{0.5}AlO_x$ and its core-shell catalysts.

Reaction conditions: 2,000 ppm propane, WHSV = 30,000 $mL \cdot g^{-1} \cdot h^{-1}$.

Fig. S11. The XRD profiles of $Pt/Ni_1Co_{0.5}AlO_x$ and its core-shell catalysts.

Fig. S12. ΔBE (eV) (difference between binding energies of the same species on different catalysts based on $Pt/Ni_1Co_{0.5}AlO_x$ catalyst) of O_{latt} and O_{ads} (a), and Co^{3+} and Co^{2+} (b) on $Pt/Ni_1Co_{0.5}AlO_x$, $Pt/Ni_1Co_{0.5}AlO_x$@ZSM-5(5%), $Ni_1Co_{0.5}AlO_x$@Pt/ZSM-5(3%), $Ni_1Co_{0.5}AlO_x$@Pt/ZSM-5(5%) and $Ni_1Co_{0.5}AlO_x$@Pt/ZSM-5(10%) catalysts.

Fig. S13. XPS full spectra (a) and Si 2p spectra (b) of $Pt/Ni_1Co_{0.5}AlO_x$ and its core-shell catalysts.

Fig. S14. Ratios of Pt^0/Pt_{total}, O_{ads}/O_{total}, Co^{3+}/Co_{total} versus T_{90} of $Pt/Ni_1Co_{0.5}AlO_x$ and its core-shell catalysts.

Fig. S15. Plot of linear correlation between H_2 consumption and H_2-TPR profile area.

Fig. S16. Profiles of the area of NH_3-TPD (a) and O_2-TPD (b) of $Pt/Ni_1Co_{0.5}AlO_x$ and its core-shell catalysts.

Fig. S17. In-situ DRIFTS spectra of propane oxidation at air (a) and at air/SO_2 (b) of $Ni_1Co_{0.5}AlO_x$@Pt/ZSM-5(3%) catalyst.

Fig. S18. The oxidative decomposition pathway of propane on the $Pt/NiCoAlO_x$.

Table S1 Pore structure parameters of $Pt/Ni_1Co_{0.5}AlO_x$ and its core-shell catalysts.

Table S2 DFT calculated geometric structural parameters of propane adsorbed on $Pt/NiCoAlO_x$ and $NiCoAlO_x$@Pt/ZSM-5 surfaces.

Table S3 Bader charge quantified state value of $Pt/NiCoAlO_x$ and $NiCoAlO_x$@Pt/ZSM-5.

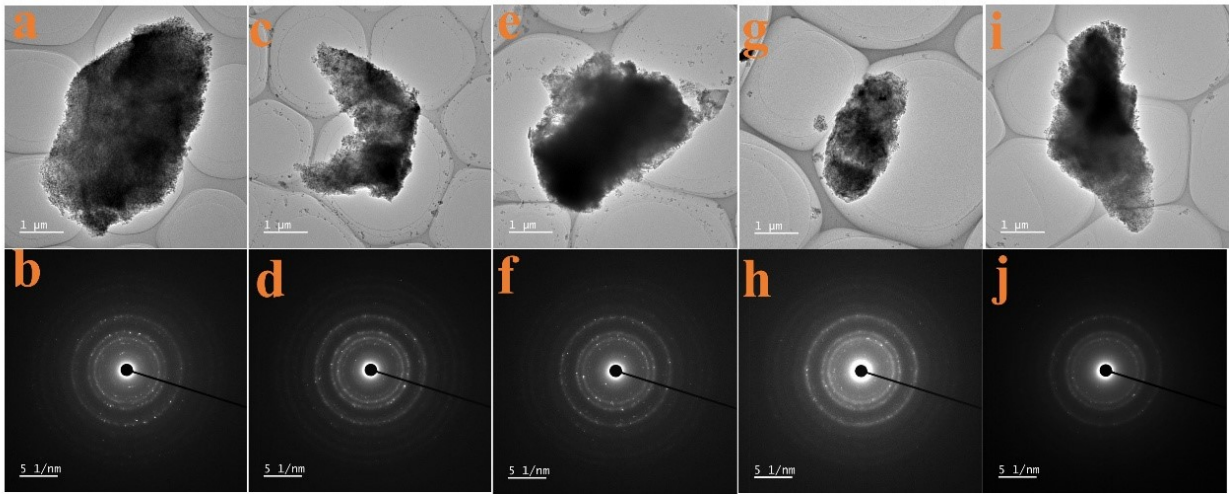

Fig. S1. TEM images of $Pt/Ni_1Co_{0.5}AlO_x$ (a and b), $Pt/Ni_1Co_{0.5}AlO_x$@ZSM-5(5%) (c and d), $Ni_1Co_{0.5}AlO_x$@Pt/ZSM-5(3%) (e and f), $Ni_1Co_{0.5}AlO_x$@Pt/ZSM-5(5%) (g and h) and $Ni_1Co_{0.5}AlO_x$@Pt/ZSM-5(10%) (i and j) catalysts.

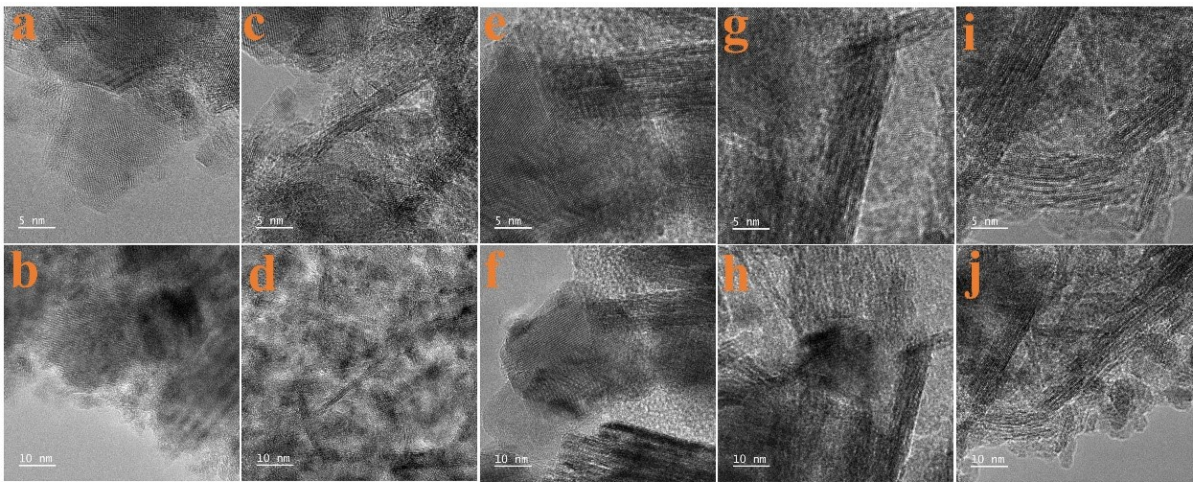

Fig. S2. HRTEM images of $Pt/Ni_1Co_{0.5}AlO_x$ (a and b), $Pt/Ni_1Co_{0.5}AlO_x$@ZSM-5(5%) (c and d), $Ni_1Co_{0.5}AlO_x$@Pt/ZSM-5(3%) (e and f), $Ni_1Co_{0.5}AlO_x$@Pt/ZSM-5(5%) (g and h) and $Ni_1Co_{0.5}AlO_x$@Pt/ZSM-5(10%) (i and j) catalysts.

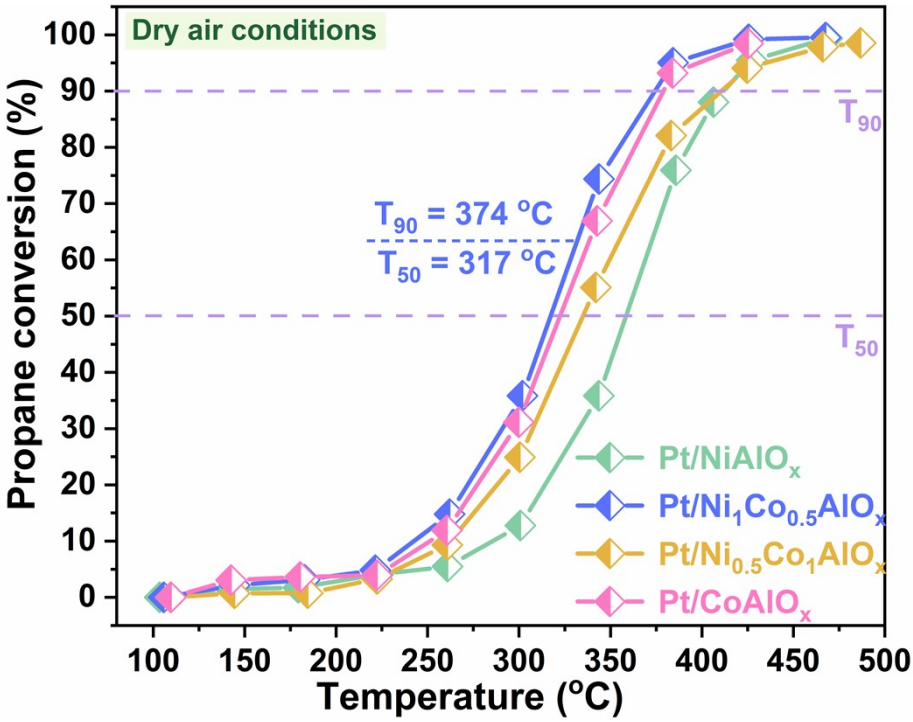

Fig. S3. The catalytic activity of $Pt/Ni_aCo_bAlO_x$ catalysts.

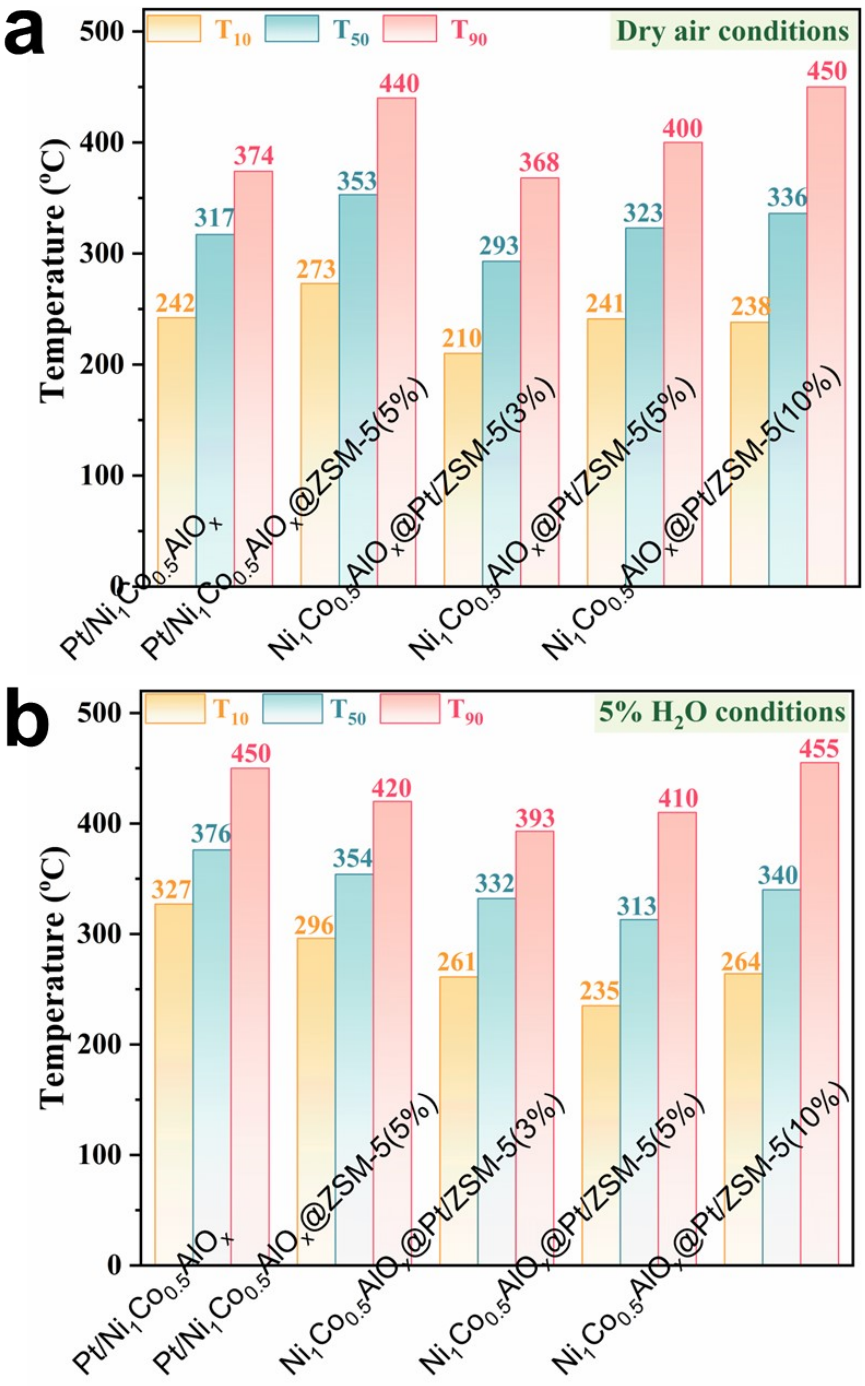

Fig. S4. Characteristic temperatures (T_{10}, T_{50} and T_{90}) of propane oxidation on $Pt/Ni_1Co_{0.5}AlO_x$ and its core-shell catalysts under dry air (a) and 5 vol% H_2O (b) conditions.

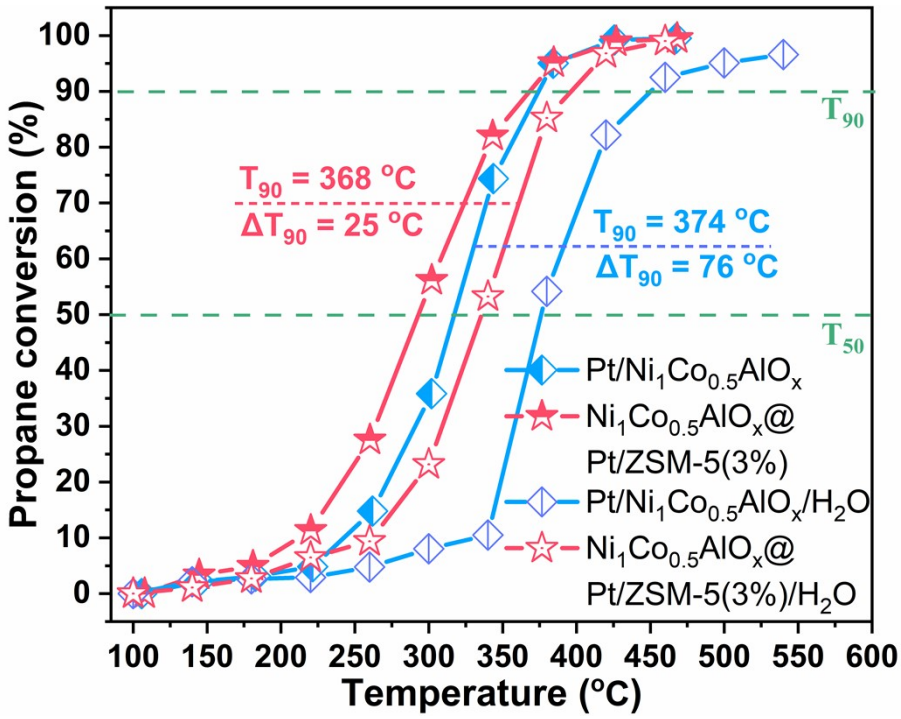

Fig. S5. Catalytic activity of $Pt/Ni_1Co_{0.5}AlO_x$ and $Ni_1Co_{0.5}AlO_x$@Pt/ZSM-5(3%) catalysts under dry air and 5 vol% H_2O conditions.

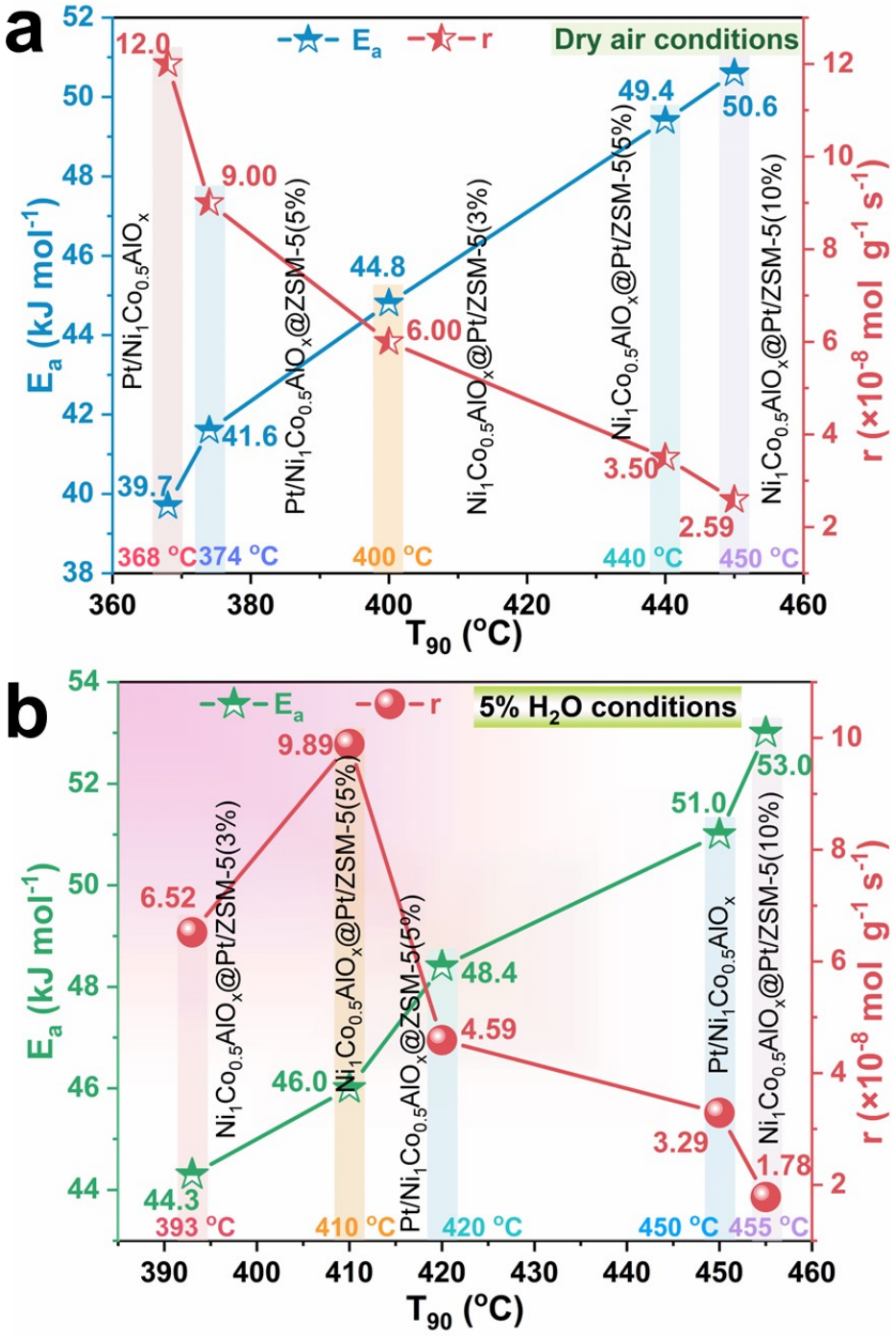

Fig. S6. E_a and reaction rate versus T_{90} of $Pt/Ni_1Co_{0.5}AlO_x$ and its core-shell catalysts under dry air (a) and 5 vol% H_2O (b) conditions.

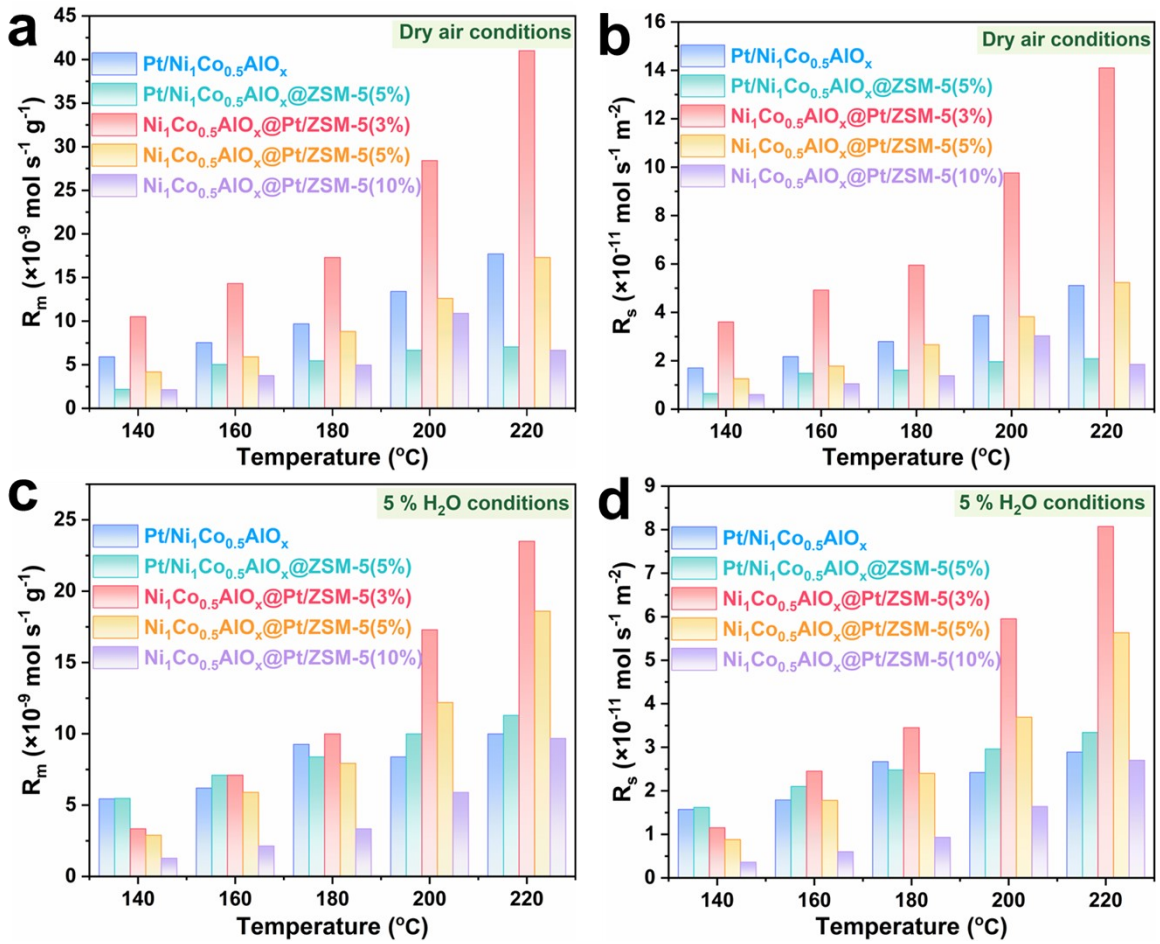

Fig. S7. R_s (reaction rates based on the specific area of catalysts) and R_m (reaction rates based on the mass of catalysts) of $Pt/Ni_1Co_{0.5}AlO_x$ and its core-shell catalysts under dry air and 5 vol% H_2O conditions.

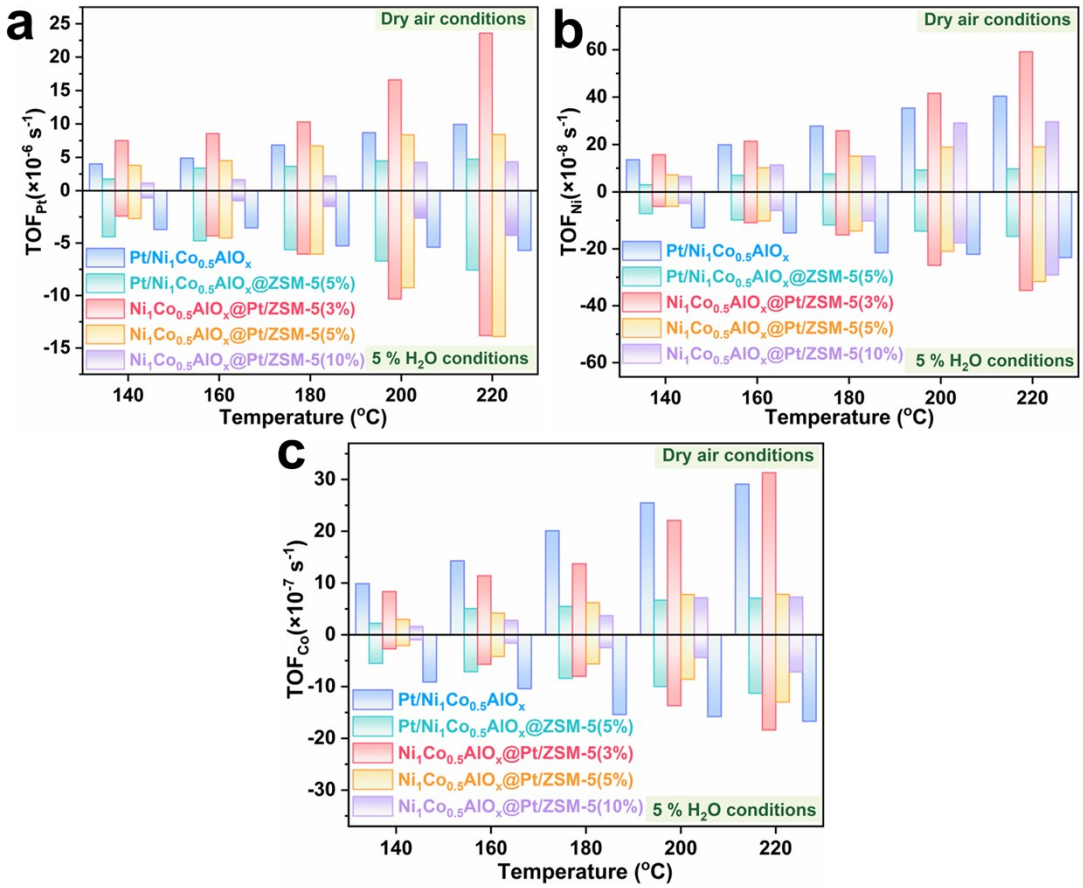

Fig. S8. TOF_{Pt} (a), TOF_{Ni} (b) and TOF_{Co} (c) values of $Pt/Ni_1Co_{0.5}AlO_x$ and its core-shell catalysts under dry air and 5 vol% H_2O conditions.

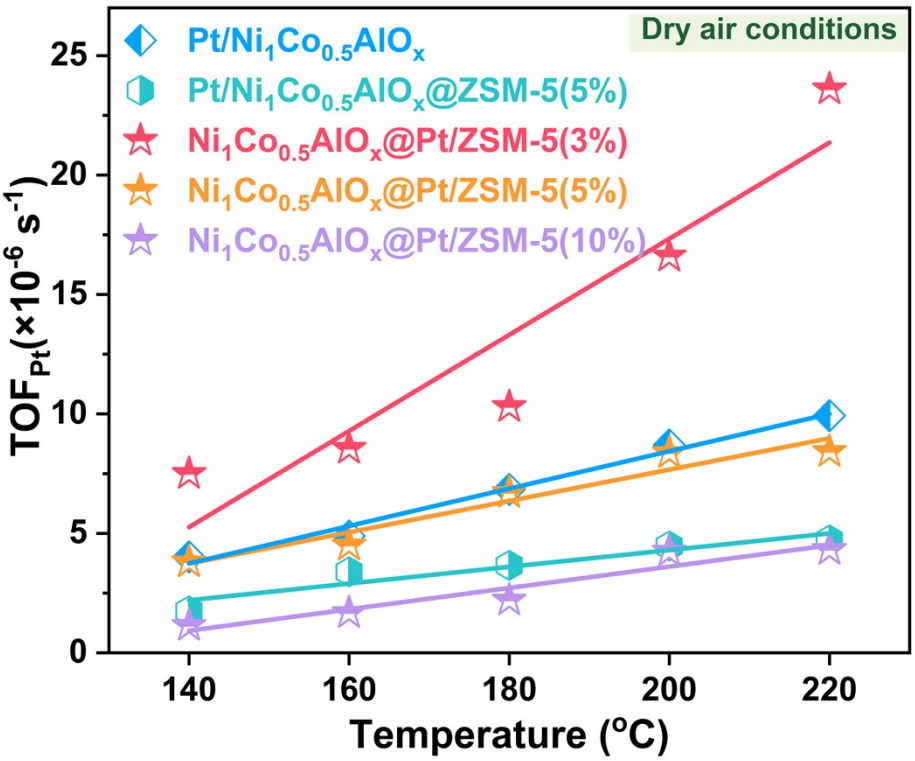

Fig. S9. TOF_{Pt} (f) of $Pt/Ni_1Co_{0.5}AlO_x$ and its core-shell catalysts under dry air conditions.

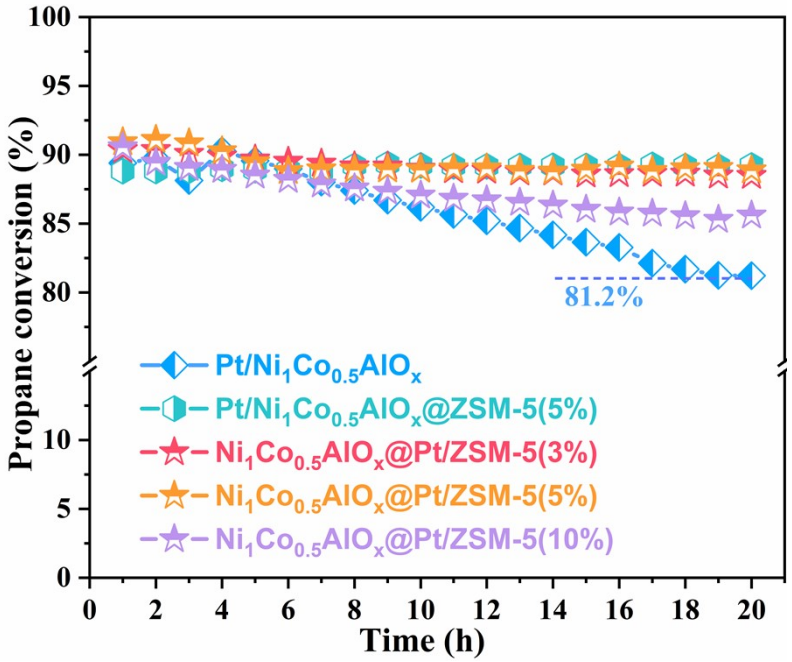

Fig. S10. The thermal stability of $Pt/Ni_1Co_{0.5}AlO_x$ and its core-shell catalysts.

Reaction conditions: 2,000 ppm propane, WHSV = 30,000 $mL \cdot g^{-1} \cdot h^{-1}$.

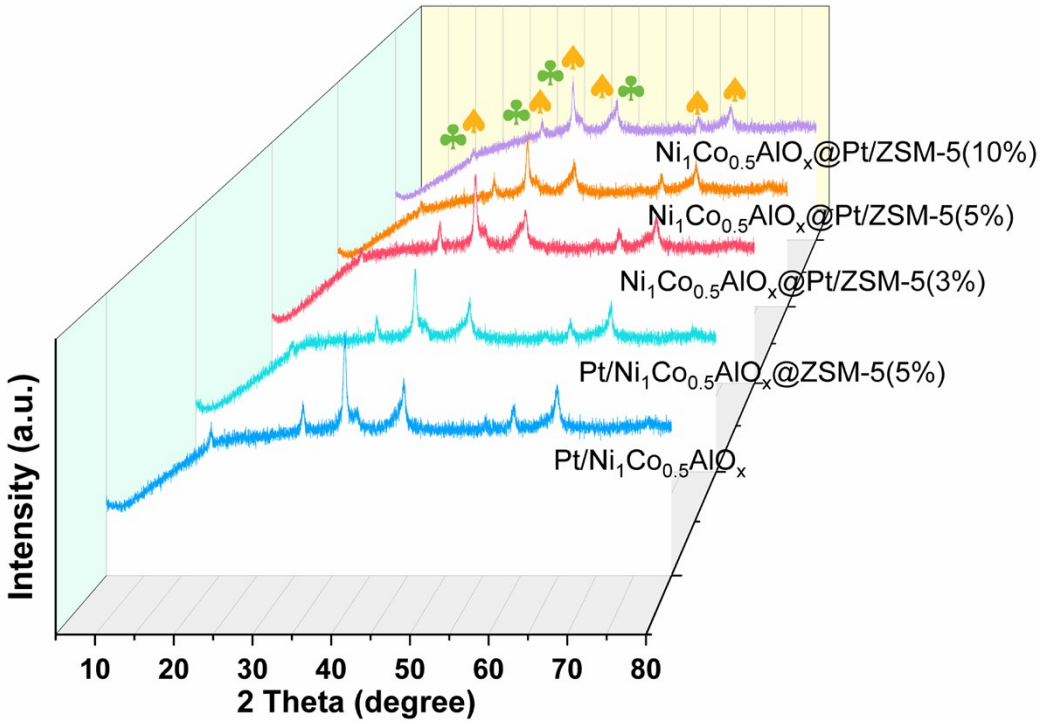

Fig. S11. The XRD profiles of $Pt/Ni_1Co_{0.5}AlO_x$ and its core-shell catalysts.

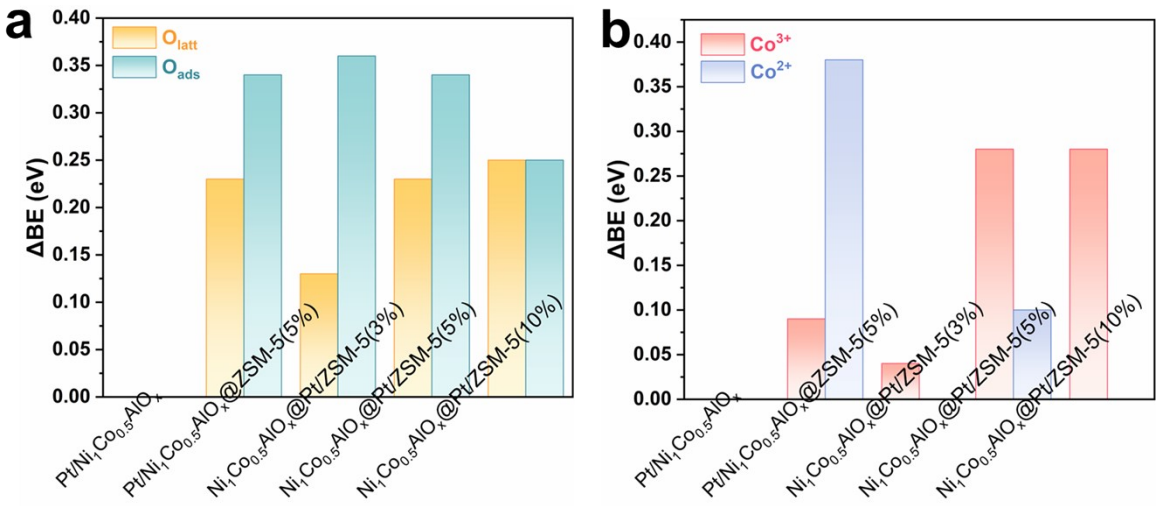

Fig. S12. ΔBE (eV) (difference between binding energies of the same species on different catalysts on basis of $Pt/Ni_1Co_{0.5}AlO_x$ catalyst) of O_{latt} and O_{ads} (a), and Co^{3+} and Co^{2+} (b) on $Pt/Ni_1Co_{0.5}AlO_x$, $Pt/Ni_1Co_{0.5}AlO_x$@ZSM-5(5%), $Ni_1Co_{0.5}AlO_x$@Pt/ZSM-5(3%), $Ni_1Co_{0.5}AlO_x$@Pt/ZSM-5(5%) and $Ni_1Co_{0.5}AlO_x$@Pt/ZSM-5(10%) catalysts.

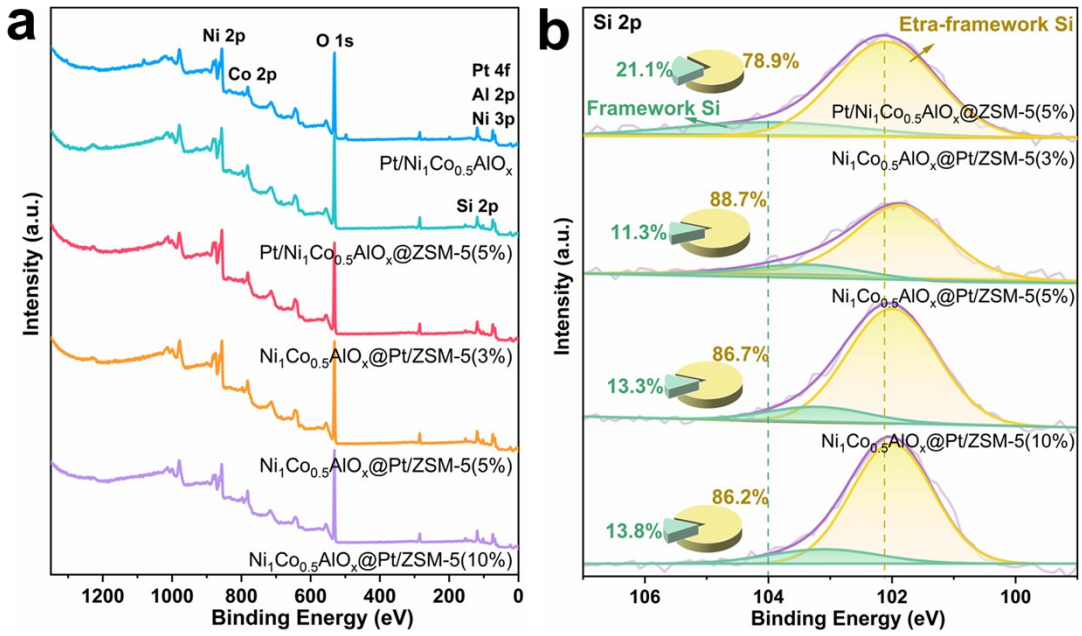

Fig. S13. XPS full spectra (a) and Si 2p spectra (b) of $Pt/Ni_1Co_{0.5}AlO_x$ and its core-shell catalysts.

The Si 2p spectra in Fig. S13 display two peaks at 101.85-102.10 eV and 103.10-104.00 eV, attributed to framework Si (mainly Si-O-Si and Si-O-Al) and extra-framework Si species, respectively. The non-polar Si-O-Si species within the ZSM-5 framework readily interact with polar water molecules, thereby conferring enhanced hydrophobicity upon ZSM-5. Following encapsulation within ZSM-5 and Pt/ZSM-5 shells, the catalyst exhibits a marked increase in Si framework content, demonstrating superior water resistance compared to the unencapsulated $Pt/Ni_1Co_{0.5}AlO_x$ catalyst.

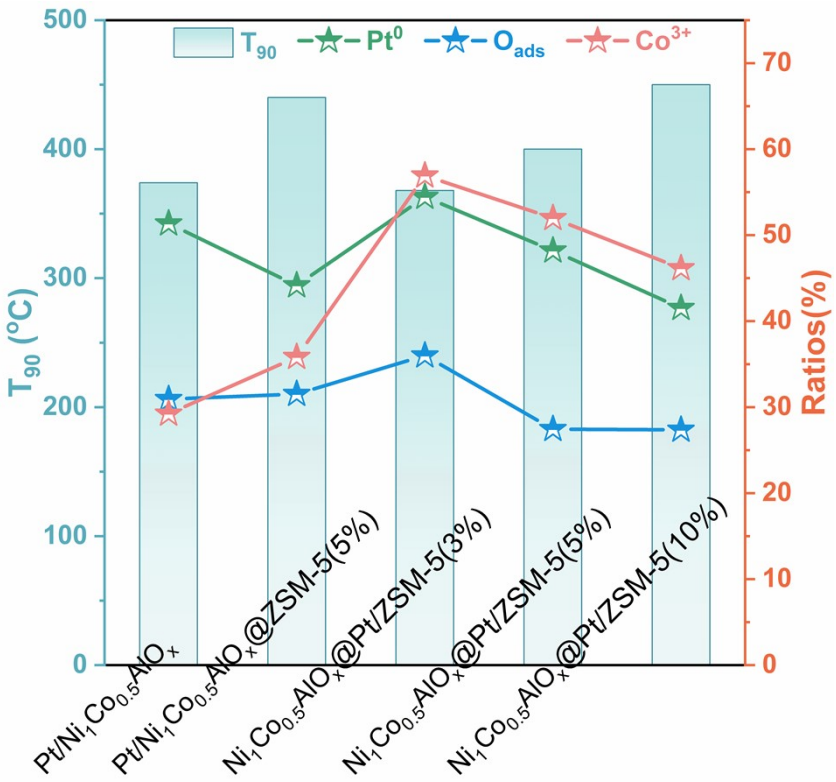

Fig. S14. Ratios of Pt^0/Pt_{total}, O_{ads}/O_{total}, Co^{3+}/Co_{total} versus T_{90} of $Pt/Ni_1Co_{0.5}AlO_x$ and its core-shell catalysts.

As shown in Fig. S14, the T_{90} value exhibits a strong negative correlation with the concentration of the primary active species, indicating that elevated levels of Pt^0, O_{ads}, and Co^{3+} significantly enhance the oxidation rate of propane at lower temperatures. These correlations highlight the pivotal contribution of these species to low-temperature catalytic performance, wherein Pt^0 provides abundant active sites for reactant activation, O_{ads} offers highly reactive oxygen for rapid oxidation, and Co^{3+} promotes redox cycling and lattice oxygen replenishment, collectively enhancing reaction kinetics.

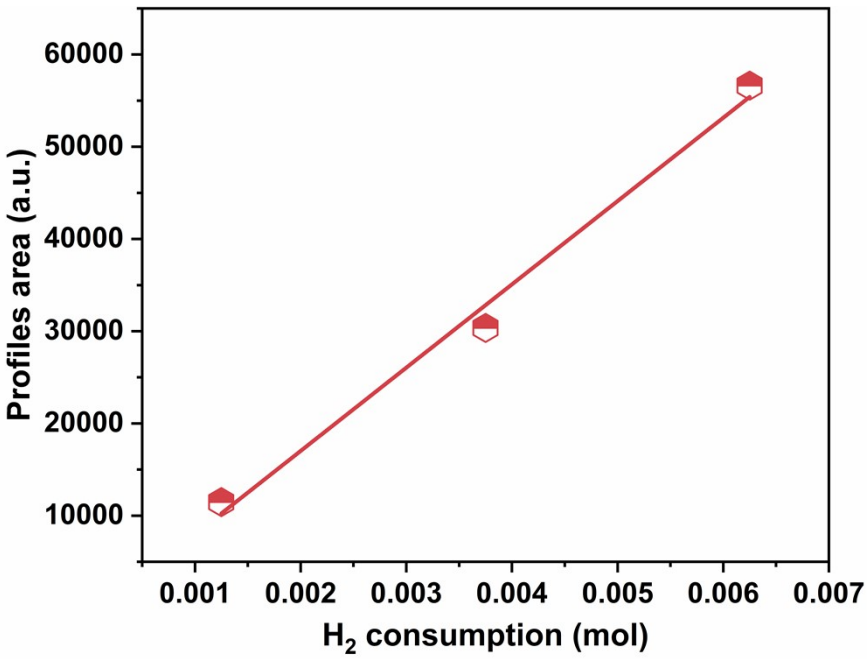

Fig. S15. Plot of linear correlation between H_2 consumption and H_2-TPR profile area.

The quantitative H_2 consumption followed the order: $Pt/Ni_{0.5}Co_1AlO_x$ (4.98 mmol/g) > $Ni_1Co_{0.5}AlO_x$@Pt/ZSM-5(3%) (4.96 mmol/g) > $Ni_1Co_{0.5}AlO_x$@Pt/ZSM-5(5%) (4.77 mmol/g) > $Pt/Ni_{0.5}Co_1AlO_x$@ZSM-5(5%) (4.73 mmol/g) > $Ni_1Co_{0.5}AlO_x$@Pt/ZSM-5(10%) (4.32 mmol/g), which is essentially consistent with the order of catalytic activity. The relatively high H_2 uptakes of $Pt/Ni_1Co_{0.5}AlO_x$ and $Ni_1Co_{0.5}AlO_x$@Pt/ZSM-5(3%) catalysts suggest superior redox capacity, facilitating C-H bond activation and thus correlating with their higher catalytic activity than other catalysts.

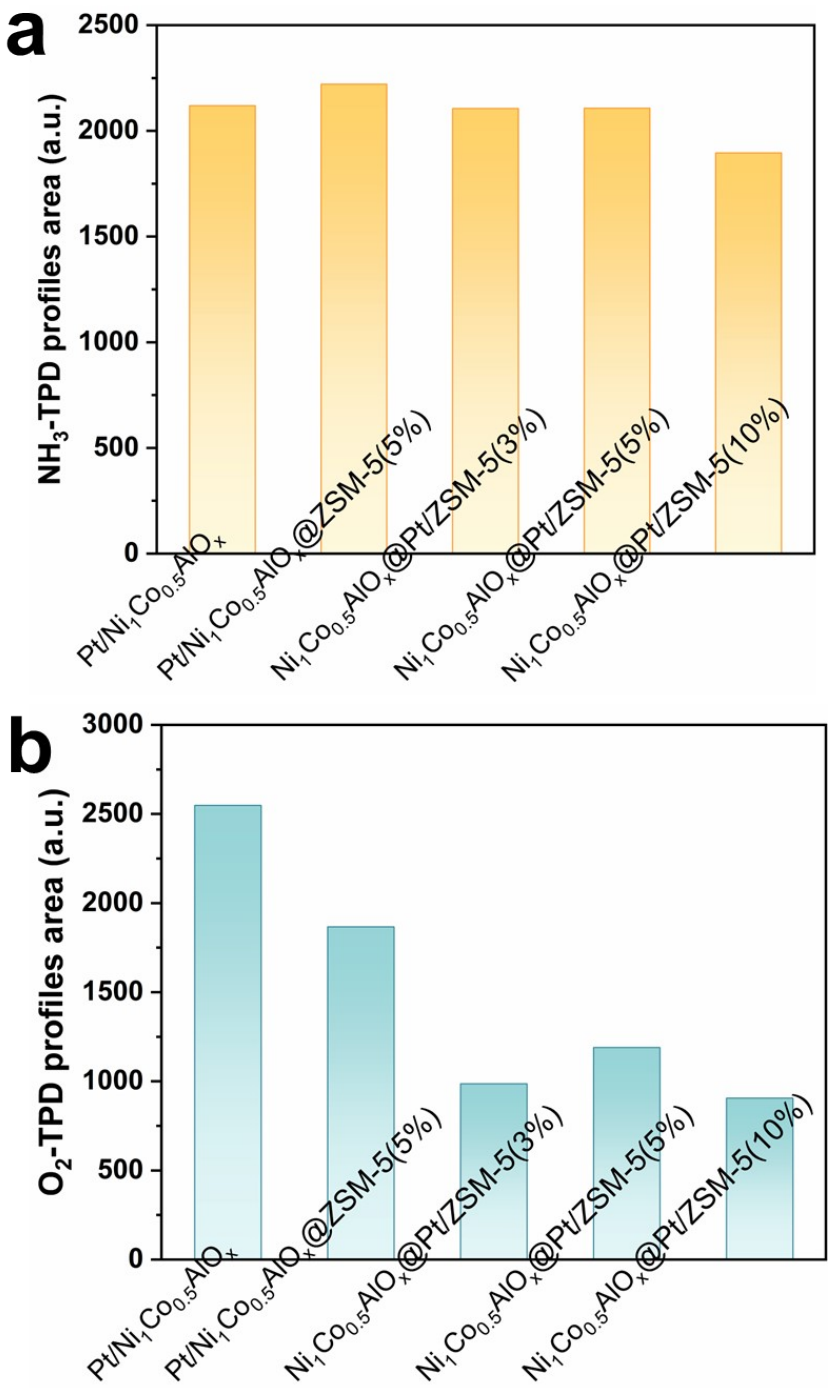

Fig. S16. Profiles of the area of NH_3-TPD (a) and O_2-TPD (b) of $Pt/Ni_1Co_{0.5}AlO_x$ and its core-shell catalysts.

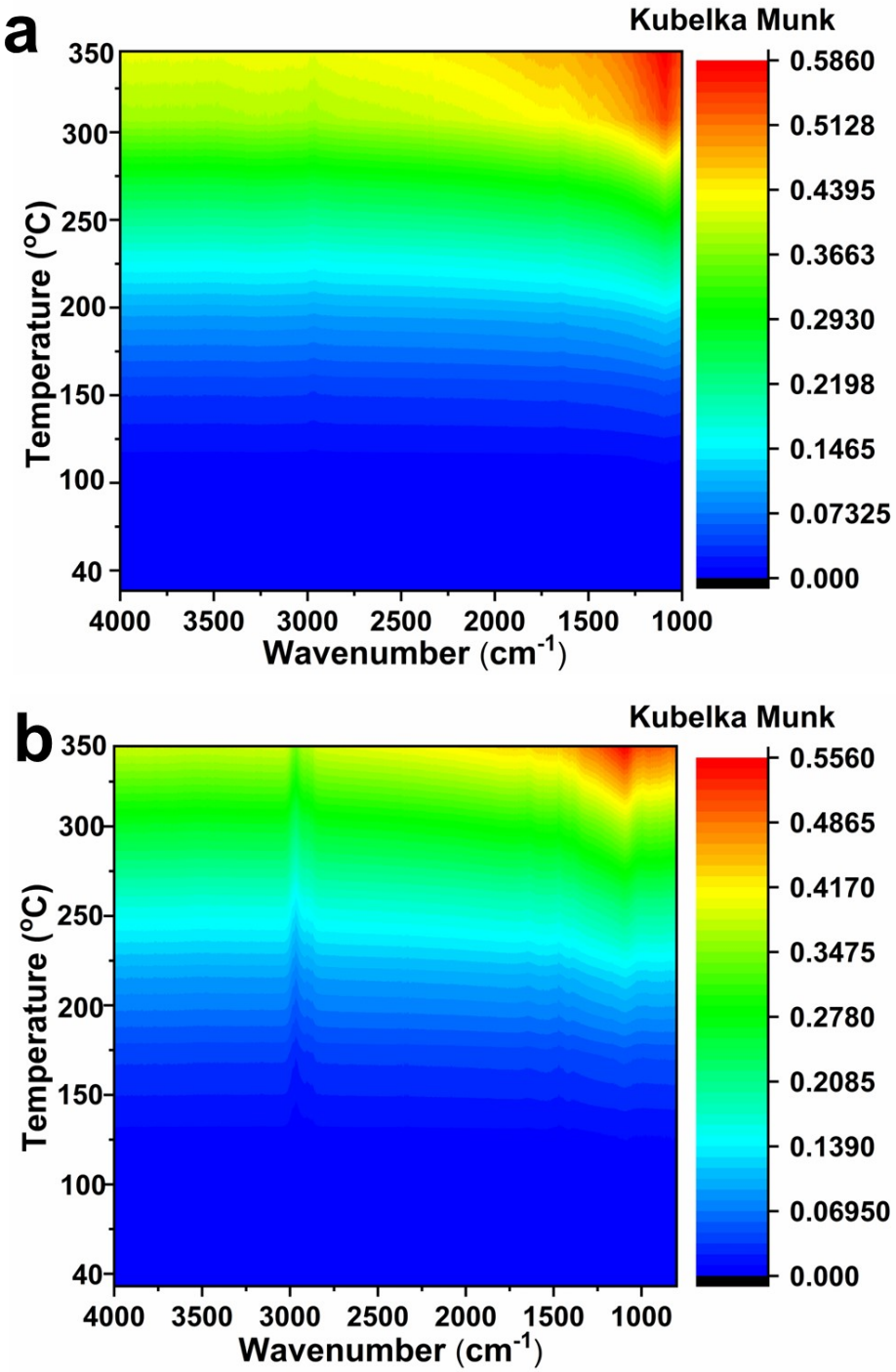

Fig. S17. In-situ DRIFTS spectra of propane oxidation at air (a) and at air/SO_2 (b) of $Ni_1Co_{0.5}AlO_x$@Pt/ZSM-5(3%) catalyst.

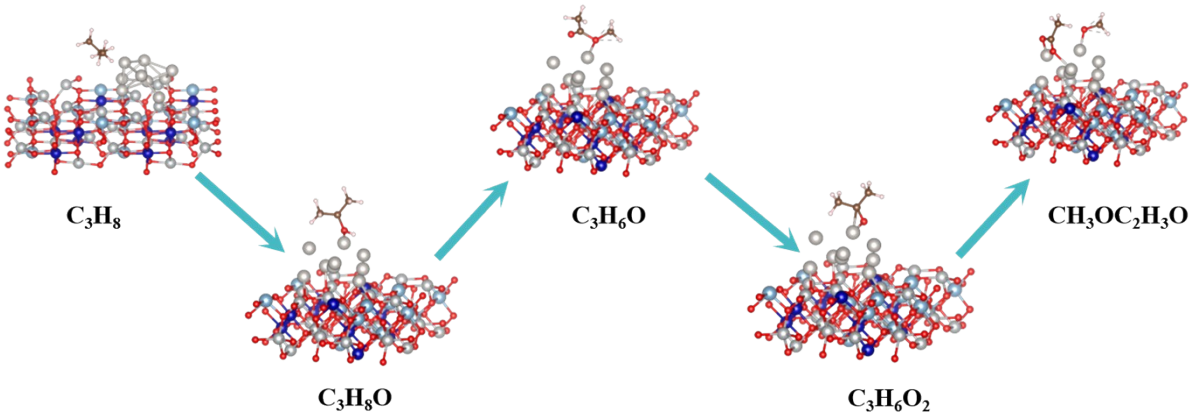

Fig. S18. The oxidative decomposition pathway of propane on the Pt/NiCoAlO_x.

Table S1 Pore structure parameters of $Pt/Ni_1Co_{0.5}AlO_x$ and its core-shell catalysts.

Catalysts	Surface area[a] (m^2/g)	Average pore size[a] (nm)	Pore volume[a] (cm^3/g)
$Pt/Ni_1Co_{0.5}AlO_x$	139	3.46	0.17
$Pt/Ni_1Co_{0.5}AlO_x$@ZSM-5(5%)	136	4.30	0.20
$Ni_1Co_{0.5}AlO_x$@Pt/ZSM-5(3%)	116	6.95	0.26
$Ni_1Co_{0.5}AlO_x$@Pt/ZSM-5(5%)	132	4.92	0.22
$Ni_1Co_{0.5}AlO_x$@Pt/ZSM-5(10%)	144	4.49	0.22

[a] Calculated using the BET method.

Table S2 DFT calculated geometric structural parameters of propane adsorbed on $Pt/NiCoAlO_x$ and $NiCoAlO_x$@Pt/ZSM-5 surfaces.

Sample	C1-C2 (Å)	ΔC1-C2 (Å)	C2-C3 (Å)	ΔC2-C3 (Å)	C1-C2-C3 (°)
C_3H_8	1.5294	--	1.5285	--	112.8815
$Pt/NiCoAlO_x$	1.5239	-0.0015	1.5223	0.0001	114.8708
$NiCoAlO_x$@Pt/ZSM-5	1.5265	0.0053	1.5258	0.0013	113.2639
Sample	C2-H4 (Å)	ΔC2-H4 (Å)	C2-H5 (Å)	C1-C2-H4(H5) (°)	C3-C2-H4(H5) (°)
C_3H_8	1.1026	--	1.1028	109.4429	109.4656
$Pt/NiCoAlO_x$	1.1020	0.0020	1.1792	107.6015	109.6308
$NiCoAlO_x$@Pt/ZSM-5	1.1078	0.1095	1.1271	108.3162	109.0214

Table S3 Bader charge quantified state value of $Pt/NiCoAlO_x$ and $NiCoAlO_x$@Pt/ZSM-5.

Sample	Electron	Average Bader charge	Average state value
$Pt/NiCoAlO_x$	Pt	9.975	0.025
	Co	7.787	2.426
	Ni	8.940	2.120
	Al	0.646	4.707
$NiCoAlO_x$@ Pt/ZSM-5	Pt	10.030	-0.030
	Co	7.727	2.546
	Ni	9.090	1.820
	Al	0.596	4.808

References

1. W. Song, C. Li, P. Ma, X. Liu, Y. Guo, M. Jia, W. Zhang, C. He, Computational screening of transition metal atom doped C_3N as electrocatalysts for nitrogen fixation, Mol. Catal., 2023, **535**, 112888.

2. X. Mao, Z. Gu, C. Yan, A. Du, Unlocking the potential of ruthenium catalysts for nitrogen fixation with subsurface oxygen, J. Mater. Chem. A, 2021, **9**, 6575-6582.

3. X. Liao, R. Lu, L. Xia, Q. Liu, H. Wang, K. Zhao, Z. Wang, Y. Zhao, Density functional theory for electrocatalysis, Energy Environ. Mater., 2021, **5**, 157-185.

4. W. Kong, J. Xu, Y. Tong, Y. Ding, J. Wang, B. Li, X. Wei, L. Zhao, Construction of dual active sites for efficient alkaline hydrogen evolution: single-metal-atoms supported on BC_2N monolayers, Phys. Chem. Chem. Phys., 2022, **24**, 29141-29150.

5. Z. Wu, M. Karamad, X. Yong, Q. Huang, D. Cullen, P. Zhu, C. Xia, Q. Xiao, M. Shakouri, F. Chen, J. Kim, Y. Xia, K. Heck, Y. Hu, M. Wong, Q. Li, I. Gates, S. Siahrostami, H. Wang, Electrochemical ammonia synthesis via nitrate reduction on Fe single atom catalyst, Nat. Commun., 2021, **12**, 2870.